Silver doped Cantor alloy thin films with tweed-like microstructure

Salah-Eddine Benrazzouq, Abdelkrim Redjaimia, Jaafar Ghanbaja, Jean-Sébastien Lecomte, Sylvie Migot, Valentin A Milichko, Jean-François Pierson

▶ To cite this version:

Salah-Eddine Benrazzouq, Abdelkrim Redjaimia, Jaafar Ghanbaja, Jean-Sébastien Lecomte, Sylvie Migot, et al.. Silver doped Cantor alloy thin films with tweed-like microstructure. Scripta Materialia, 2025, 258, pp.116521. 10.1016/j.scriptamat.2024.116521 . hal-04855982

HAL Id: hal-04855982
https://hal.science/hal-04855982v1

Submitted on 26 Dec 2024

Scripta Materialia 258 (2025) 116521

Contents lists available at ScienceDirect

Scripta Materialia

journal homepage: www.journals.elsevier.com/scripta-materialia

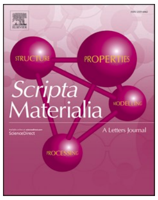

Silver doped Cantor alloy thin films with tweed-like microstructure

Salah-Eddine Benrazzouq [a], Abdelkrim Redjaimia [a], Jaafar Ghanbaja [a], Jean-Sébastien Lecomte [b], Sylvie Migot [a], Valentin A. Milichko [a], Jean-François Pierson [a,*]

[a] *Université de Lorraine, CNRS, IJL, F-54000 Nancy, France*
[b] *Université de Lorraine, CNRS, ENSAM, LEM3, F-57000 France*

ARTICLE INFO

Keywords:
High entropy alloys
Thin films
Magnetron sputtering
Microstructure
Spinodal decomposition
Precipitation

ABSTRACT

We report on the effect of silver doping on the microstructure of Cantor alloy thin films deposited by magnetron co-sputtering. The introduction of silver, with its higher enthalpy of mixing exceeding the thermodynamic criterion for stable solid solutions, promotes the coexistence of a crystallized silver face-centered cubic (fcc) phase alongside the Cantor phase. Using X-ray diffraction, scanning and transmission electron microscopy, and energy-dispersive X-ray spectroscopy, alongside with thermodynamic modeling through the CALPHAD methodology, we provide a comprehensive analysis of the resulting tweed-like microstructure. The findings underscore the substantial impact of compositional modifications on the microstructural development of high entropy alloys for their diverse applications.

Over the past two decades, there has been a growing focus on multicomponent alloys, with a special attention on engineering of unique microstructures to tune their properties [1]. High entropy alloys (HEAs), as one of such alloys, are generally described as a mix of five or more elements with concentrations ranging from 5 to 35 at % [2,3]. Due to unconventional compositions and chemical structures of HEA, they demonstrate exceptional mechanical properties [4], such as excellent wear resistance [5,6], high strength, strong resistance to fatigue and fracture [7,8], and good corrosion and oxidation resistance [9]. HEAs also have a distinctive combination of magnetic and electrical properties [10,11], which make HEAs potentially attractive materials for catalysis [12,13], energy storage [14], biomedical [15] and hard coatings [16].

Generally, HEAs possess face-centered cubic (fcc) [17], body-centered cubic (bcc) [18], hexagonal close-packed (hcp) structures [19], or a combination of fcc/bcc solid solution (SS) phases [20], that distinguish them from brittle intermetallic compounds (IMCs). However, next to single-phase in HEAs, multiple principal elements provide HEA to undergo phase separation, including spinodal decomposition [21], and the formation of second-phase nano-precipitates [22–24]. The formation of such a second phase is influenced by the competition between the high configurational entropy of mixing ($\boldsymbol{\Delta S_{mix}^{conf}}$), and the enthalpies of mixing ($\boldsymbol{\Delta H_{mix}}$) [25]. Consequently, the same HEA may exhibit a single-phase SS at high temperatures, but decomposes into two phases at low temperatures. As a result, the HEAs microstructures formed can be highly complex and hierarchical, spanning multiple length scales [24]. As an example, several studies showed that the additions of another element (such as Al, Mo, Ti, V or Nb) into representative Cantor alloy (CrMnFeCoNi) may have a strong effect on the structure, microstructural (morphology) and the subsequent functional properties [26–31]. However, the fundamental thermodynamic driving forces beyond the formation of SS in HEAs are still not clearly understood.

To address this issue, some empirical thermodynamic, steric, electronics and chemical criteria to predict the presence or absence of SS in HEAs should be considered. According to several experiments, the single phase SS in HEAs is driven by the following thermodynamic parameters ($\boldsymbol{\Delta H_{mix}}$ ***and*** $\boldsymbol{\Delta S_{mix}^{conf.}}$) and the relative atomic size displacement (δ) [32,33] rules: $\Delta S_{\mathrm{mix}} > 13.38$ J mol^{-1} K^{-1}, -10 kJ mol^{-1} $< \Delta H_{\mathrm{mix}} < 5$ kJ mol^{-1}, and $\delta < 4$ %. Based on these relationships, we investigated an effect of Ag introduction to Cantor alloy on their structure and microstructure. Silver has been selected because its enthalpy of mixing is higher than the thermodynamic criteria of 5 kJ mol^{-1}, which potentially induces the lattice distortion and the formation of new nano-precipitated phases, enhancing thus the alloy's mechanical properties and performance [34]. For this, a series of $(\mathrm{CrMnFeCoNi})_{100\text{-}x}\mathrm{Ag}_x$ HEAs thin films were deposited using magnetron co-sputtering. Their chemical compositions, structure, and microstructure were analyzed, along with correlations with thermodynamic calculations using the

---

* Corresponding author.
E-mail address: jean-francois.pierson@univ-lorraine.fr (J.-F. Pierson).

https://doi.org/10.1016/j.scriptamat.2024.116521
Received 1 July 2024; Received in revised form 1 October 2024; Accepted 15 December 2024
Available online 20 December 2024

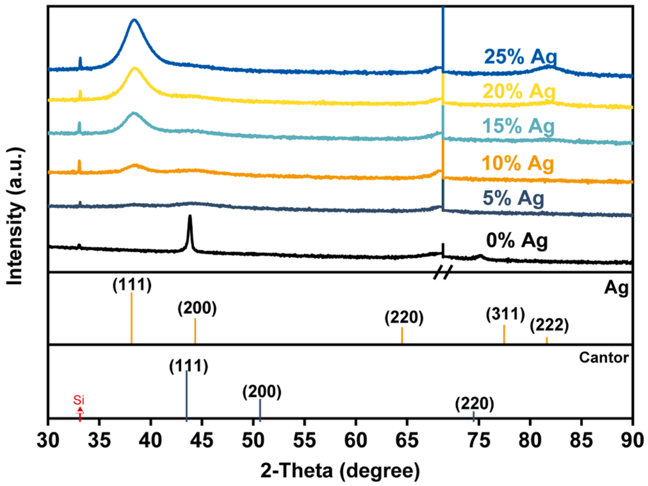

Fig. 1. X-ray diffractogram of CrMnFeCoNi (Cantor alloy) thin films with progressive addition of Ag.

Thermocalq® software based on CALPHAD (CALculated PHAse Diagram) phenomenological approach. In addition, a heat treatment in vacuum was employed to study the effect on the evolution of the nano-precipitated microstructure. The findings underscore the substantial impact of compositional modifications on the microstructural development of high entropy alloys for their diverse applications.

As a reference HEA, the equiatomic CoCrFeMnNi system, known as the Cantor alloy, was selected [35]. Generally, the Cantor HEA thin films deposited using magnetron sputtering exhibit a high hardness of 8.9 GPa that can be improve up to 13.8 GPa after annealing at 450 °C, as compared with a hardness of 2.5 GPa for its bulk counterpart and reach a maximum after deformation of 6.5 GPa [36,37].

CrMnFeCoNi$_{(100\text{-}x)}$Ag$_x$ (with $0 < x < 25$ at %) thin films were deposited using DC magnetron co-sputtering of CrMnFeCoNi target and Ag one (both targets having a purity higher than 99.99 %) on (100) Si substrate. Prior to the deposition, the Si substrates underwent cleaning with acetone and 5-minutes etching in an argon radiofrequency plasma. Both targets were pre-sputtered during 5 min to eliminate impurities and oxides from their surfaces. During the deposition, the argon gas flow rate was set at 30 sccm (standard cubic centimeters per minute), and the substrate rotation rate was maintained at 15 rpm (rotation per minute) to ensure homogeneity in film composition and thickness. The two cathodes were arranged in a confocal configuration, with a target-substrate distance of 9 cm, and the working pressure was kept at 0.3 Pa. All deposition procedures were conducted for 40 min at ambient temperature in a vacuum chamber with a base pressure of 1.0×10^{-7} mbar. The Ag-content was adjusted by controlling the DC current applied to the Ag target, while the DC current applied to the CrMnFeCoNi target was set at 0.4 A. Depending on the silver concentration, the thickness of the deposited films was ranging between 820 and 1200 nm. Then, the film containing 10 at.% of Ag was thermally treated at 400 °C during 2 h under vacuum (10^{-7} mbar), followed by slowly cooling under vacuum to avoid oxidation.

X-ray diffraction (XRD) analyses was performed in the Bragg–-Brentano configuration with Cu Kα radiation ($\lambda = 1.5406$ Å) using an AXS Bruker D8 Advance diffractometer. Transmission electron microscopy (TEM) was carried out using a JEOL - ARM 200F Cold FEG TEM/STEM operating at 200 kV and equipped with a spherical aberration (Cs) probe and image correctors (point resolution of 0.12 nm in TEM mode, and 0.078 nm in STEM mode). Energy-dispersive X-ray spectroscopy (EDS) analysis was performed in STEM mode using a Centurio silicon drift detector (SDD) that collects X-rays from STEM samples at a large solid angle of up to 0.98 srd from a detection area of 100 mm^2. Cross-section TEM samples were prepared using a focused ion beam (FIB)-scanning electron microscope dual-beam system (FEI Helios NanoLab 600i). Scanning electron micrographs (SEM) of the HEA thin films were captured in both top and cross-section views using a ZEISS GeminiSEM 500 with an accelerating voltage of 5 kV. The film hardness has been measured by nanoindentation with Berkovich diamond indenter (UHNT Anton Parr, Austria). The instrument was calibrated using a standard fused silica specimen. Load (P) vs. indentation depth (h) measurements were carried out in force-controlled mode with an applied load fixed at 1000 μN, resulting in a penetration depth of approximately 90 nm (well below 1/10th of the film thickness). Each test involved a 3×3 array of indents with a spacing of 10 μm in both ‘x’ and ‘y’ directions, and the average value of these measurements was used for data interpretation.

Thermodynamic calculations were conducted using CALPHAD method (SSOL database) to predict the phase stability. Phase diagrams of the alloy were generated, specifically at Ag concentrations of 0, 5, 10, 15, 20, and 25 at.%, in order to determine the phases present in each sample at specified temperatures.

The X-ray diffractograms of CrMnFeCoNi HEA thin films at various Ag concentration are presented in Fig. 1. We revealed diverse phases from a well crystallized fcc phase of Cantor with a preferred orientation along the <111> direction at 0 at.% Ag, to a mixture of fcc Ag and fcc

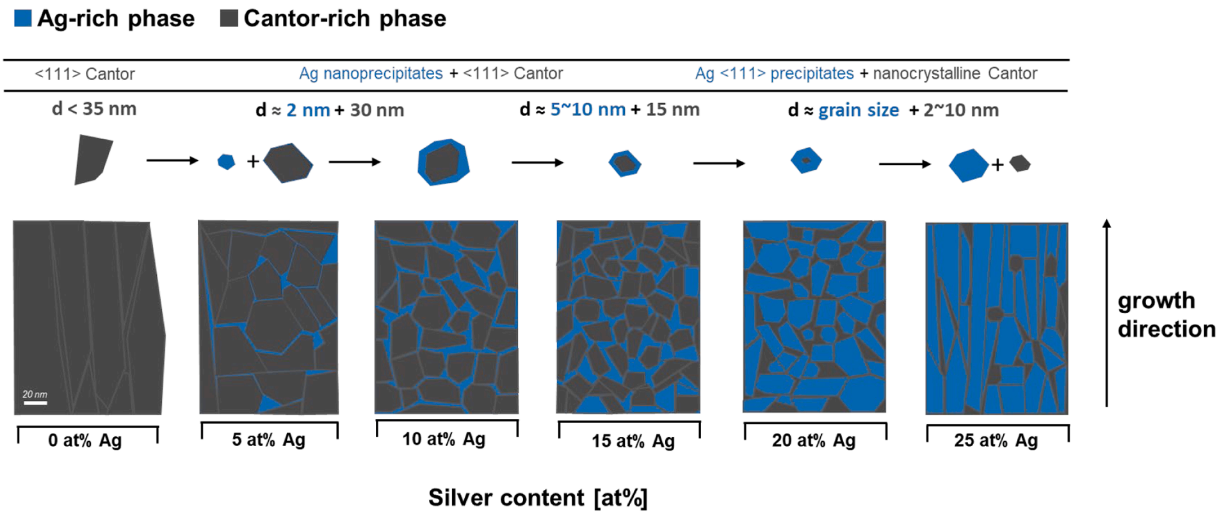

Fig. 2. Schematic illustration of microstructural evolution in the Cantor alloy thin film with increasing silver content: transition from well-crystallized fcc Cantor phase to nanocrystalline Cantor with well-crystallized fcc silver phase.

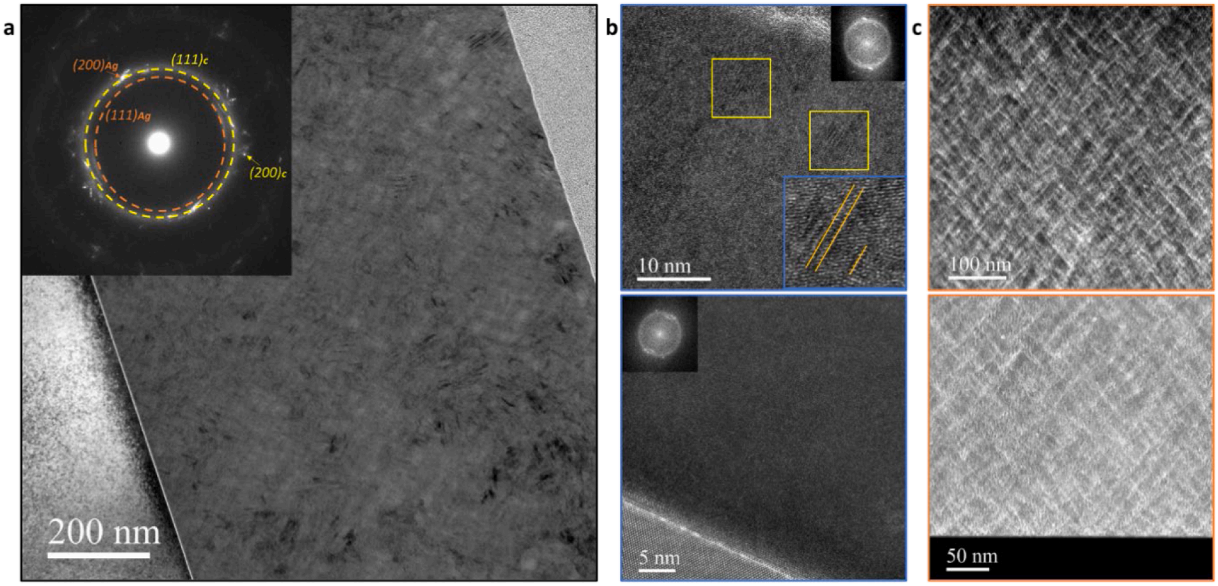

Fig. 3. (a) Bright-field transmission electron microscopy (BF-TEM) micrograph and corresponding selected area (inset) electron diffraction (SAED) pattern for the Cantor alloy thin film with 10 at% Ag. (b) High resolution TEM (HRTEM) micrographs and corresponding Fast Fourier Transform (FFT). (c) High angle annular dark field STEM (HAADF STEM) micrographs.

Cantor phase at 5 at.% Ag and more. Herein, the XRD disclosed a distinct non-mixing behavior of Ag with the Cantor alloy. In more details, when the Ag content is fixed to 5 at %, the (111) diffraction of the Cantor phase is broadened while a new peak appears close to 38° corresponding to the (111) Ag diffraction plane. The increase of the Ag content leads to an increase of the intensity of this peak. Consequently, addition of Ag into Cantor thin films favors the formation of the Ag phase over the Cantor one. Thus, XRD analysis suggests that the films containing Ag are biphased: an X-ray amorphous (or poorly crystallized) Cantor phase and a nanocrystallized Ag-based phase. Such biphased microstructure indicates that the growth of one of these phases is disrupted by the growth of the other one. To clarify the mechanism by which silver addition leads to the amorphization of the Cantor alloy, we conducted a detailed illustration of the microstructural evolution with increasing Ag content. Fig. 2 illustrates this process schematically. As Ag is introduced into the Cantor alloy matrix, it initially segregates to form nanoscale precipitates. These precipitates create local lattice distortions due to the size mismatch between Ag atoms and the Cantor elements. As the Ag content increases, these distortions become more pronounced and extensive, disrupting the long-range order of the Cantor fcc phase. This disruption is further extended by the tendency of Ag to form its own fcc phase, which competes with the Cantor phase for stability. The result is a gradual transition from a well-crystallized fcc Cantor phase to an increasingly disordered structure, eventually leading to an X-ray amorphous state at higher Ag concentrations.

The surface morphology of the films observed by SEM is depicted in Figure S1 as a function of the Ag content. The top-view micrograph of CrMnFeCoNi exhibits a granular and smooth microstructure. Notably, a discernible microstructural change occurs with the increasing Ag content: Ag nanoparticles are observed to be well-distributed on the top surface of the films; while as the Ag content increases, both density and size of these nanoparticles increase, being confirmed also by XRD.

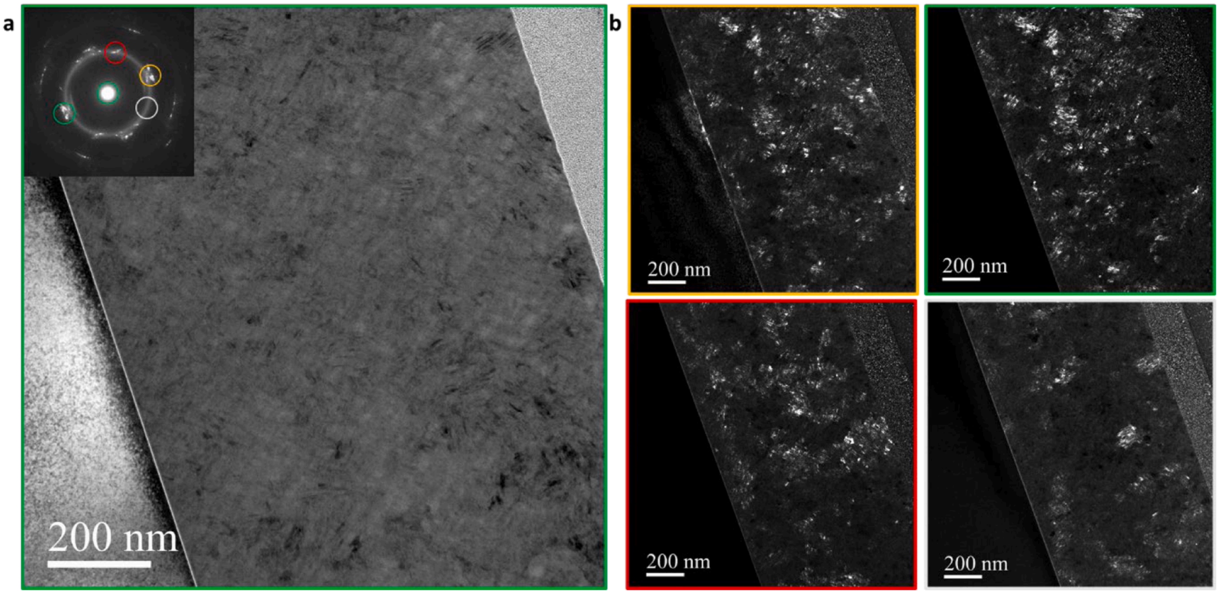

Fig. 4. (a) BF-TEM micrograph and corresponding SAED pattern for the Cantor alloy thin film with 10 at% Ag. (b) Dark field TEM micrographs.

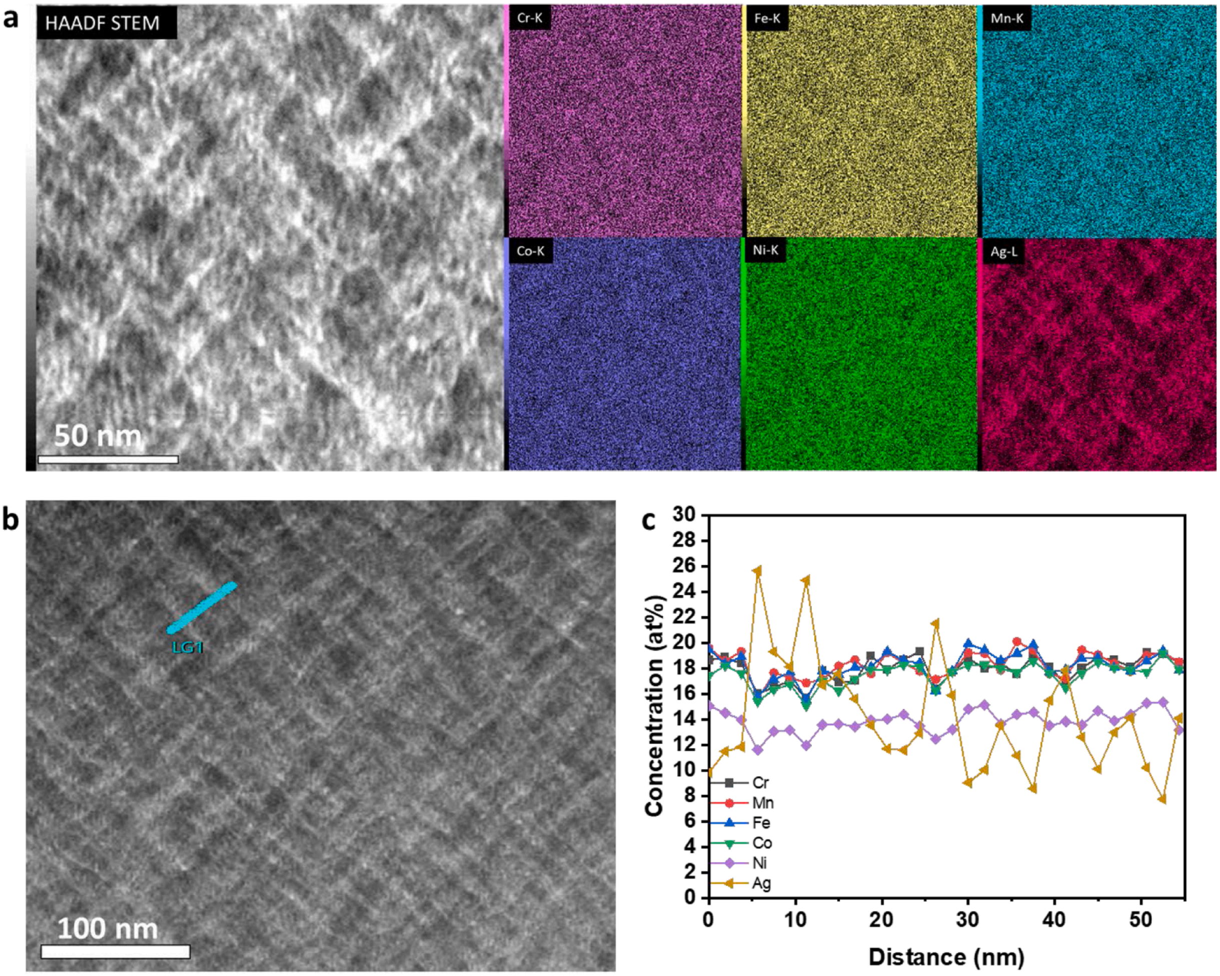

Fig. 5. (a) HAADF-STEM micrograph and the corresponding STEM-EDS elemental maps of Cr, Mn, Fe, Co, Ni, and Ag. (b-c) Line-scan EDS profile of atomic fraction of individual elements.

For a more detailed insight, cross-sectional SEM images of CrMnFeCoNi thin films with various Ag contents are provided in Figure S2. These micrographs revealed a columnar microstructure for the pure Cantor film. Further addition of Ag induced denser films, with the emergence of a vein-like pattern structure [38]. This intricate structure is distinctly visible on the fracture surface of metallic glasses [39]. The evolving microstructural features, both on the top surface and in cross-section, signify the impact of increasing Ag content on the morphology and organization of the HEA thin films. The vein-like patterns observed in the denser microstructure suggest a complex interplay of Ag within the alloy, contributing to the overall structural evolution.

To investigate the detailed microstructure and phase evolution of CrMnFeCoNiAg HEA thin films, the sample containing 10 at.% Ag has been characterized by TEM. Fig. 3a displays cross-section bright-field TEM images and corresponding selected area electron diffraction (SAED) patterns of the as-deposited CrMnFeCoNiAg HEA thin films. According to the XRD results presented in Fig. 1, this film primarily contains two phases: fcc phase of Cantor and fcc of Ag. The 900-nm-thick film exhibits a distinct dense structure with clearly identifiable areas referring to Ag precipitates distributed throughout the entire thickness. The SAED pattern confirms the presence of both Ag and Cantor phases, with bright spots corresponding to the (200) diffraction plane of Ag and the (200) diffraction plane of Cantor. Herein, the observed diffused rings indicate a nanocrystalline phase in both (111) diffraction planes for Cantor and Ag.

High-resolution TEM (HRTEM) micrographs (Fig. 3b) taken at the top and bottom of the film reveal a nanocrystalline morphology with fine-scale linear precipitates, as confirmed by fast Fourier transform (FFT) patterns. Scanning transmission electron microscopy-high-angle annular dark-field (STEM-HAADF) imaging was employed to eliminate diffraction contrast and to highlight the internal structure of the thin film (Fig. 3c). In this mode, the image contrast depends solely on differences in atomic number. Herein, a characteristic modulated pattern is observed, with two sets of striations parallel to the basal plane. Indeed, similar modulated structures featuring cuboidal particles or tweed-like contrast patterns was revealed using TEM in many alloys [40–43]. These observations are frequently associated with the uniform and coherent precipitation of a second phase characterized by a lattice misfit, as outlined by Wagner and Kampmann in 1991 [44]. A relatively high lattice misfit is necessary for an alloy to display spinodal decomposition-based structures. The reported HEA system with a similar spinodal microstructure has a lattice misfit higher than 0.5 % [21,40,45]. Typically, the striations align parallel to the soft directions of an elastically anisotropic matrix, indicating a tendency to minimize the overall elastic strain energy [46], it could be stated that the CrMnFeCoNiAg thin film with 10 at.% silver concentration consists of a mixture of 2 phases: CrMnFeCoNiAg matrix and almost pure Ag nanoprecipitates is the bright striation. Dark-field TEM micrographs in Fig. 4 illustrate the distribution of nanoprecipitates (bright) in the CrMnFeCoNiAg alloy, confirming that the Ag nanoprecipitates are within the Cantor matrix.

STEM-EDX mapping analysis (Fig. 5a) demonstrates that the chemical composition of the film remains homogeneous for all Cantor's elements, but a modulated pattern is observed for Ag, with more silver in

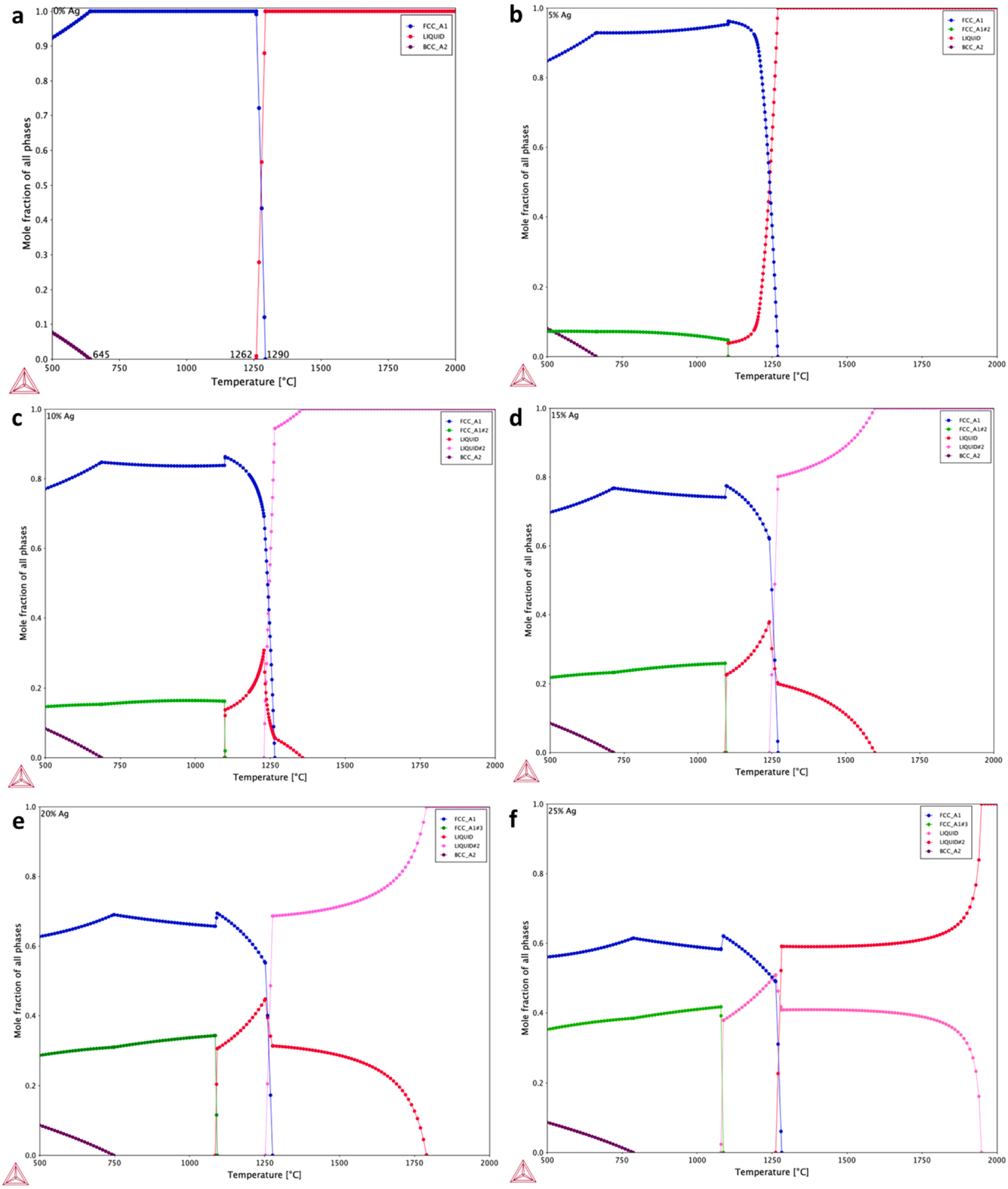

Fig. 6. Solidification path for Cantor$_{100\text{-}x}$Ag$_x$ alloys calculated under equilibrium conditions using Lever Rule Equations (Thermocalq® Software). The concentration (*at.* %) are indicated in the top left of the phase diagrams (a) 0 at% Ag, (b) 5 at% Ag, (c) 10 at% Ag, (d) 15 at% Ag, (e) 20 at% Ag, (f) 25 at% Ag.

the corners and less in the center. To determine this change in nanoprecipitate composition, STEM-EDX profile line analysis (Fig. 5b and c) of the modulated pattern was performed. The analysis reveals a higher silver content in the corners, approximately 26 at%, decreasing towards the center of the pattern to approximately 8 at%, taking into account the thickness of the FIB lamella, while the Cantor element remains constant.

To investigate the influence of temperature on the microstructural evolution of the (CrMnFeCoNi)$_{90}$Ag$_{10}$ thin films, we conducted annealing experiments at 400 °C for 2 h. This temperature was chosen to allow substantial atomic diffusion while remaining below the point of major phase transformations. Upon annealing at 400 °C, we observed significant microstructural changes, as illustrated in Figures S3, S4, and S5. The XRD results (Figure S3) reveal the emergence of well-defined peaks corresponding to the Ag fcc structure, indicating enhanced crystallization of the Ag phase. This crystallization is driven by the increased atomic mobility at elevated temperatures, allowing Ag atoms to diffuse and form larger, more coherent domains. The microstructure formed is similar to that observed under normal conditions but with channels starting to project at the intersections like nodes that are periodically arranged. This projection seems to be associated with the contraction of the Cantor channels at the center, between the nodes, and Ag in the nodes (Figure S4). Additionally, Figure S5 displays an EDX map analysis revealing that adjacent Ag-domains are separated by Cantor channels at the center, and the domains of Ag are bigger compared to normal conditions. Furthermore, the line profile indicates that the Ag content in the Ag-rich regions increases dramatically, reaching up to 45 at.%, compared to the initial 10 at.% in the as-deposited film.. This significant increase in the Ag-content suggests a substantial redistribution of elements within the alloy, which is consistent with a spinodal decomposition mechanism where the alloy separates into distinct phases with different compositions during annealing. The presence of a miscibility gap in this senary alloy system is possibly associated to the strong miscibility gaps present between silver and cantor elements, as supported by our thermodynamic calculations, one can notice that the ($\boldsymbol{\Delta H_{Ag}^{X}}$) of atom-pairs of Ag and the atoms of the Cantor alloy are all positive. This indicates that the Ag atoms have very low affinity with the atoms inside the Cantor alloys. This favors the precipitation of pure Ag or a little bit associated with Cantor elements in the Cantor matrix (Figure S6).

The hardness of Cantor alloy thin films is approximately 8.3 ± 0.5 GPa. The addition of silver initially decreases the hardness to about 5 GPa due to the formation of a soft, silver-rich phase. However, thermal treatment of the 10 at.% Ag film at 400 °C for 2 h dramatically increases the hardness to 12.9 ± 0.7 GPa. This 158 % increase can be attributed to the observed spinodal-like decomposition, resulting in a nanocomposite structure with Ag-rich regions (up to 45 at.% Ag) separated by Cantor-rich channels. This microstructure likely enhances hardness through coherency strain, increased obstacles for dislocation motion, and possible grain refinement.

To investigate the chemical states of the constituent elements after thermal treatment, we performed Electron Energy Loss Spectroscopy (EELS) analysis on the $(CrMnFeCoNi)_{90}Ag_{10}$ annealed thin film. Figure S7 presents the EELS spectra for Cr, Mn, Fe, Co, Ni, and Ag, alongside reference spectra for their respective metallic state standards. The results consistently show that all elements in our annealed sample maintain their metallic states, with spectral features closely matching those of the pure metallic standards.

To validate our experimental results, we employed thermodynamic modeling through the Calculation of Phase Diagram (CALPHAD) approach, using Thermocalc software and the SSOL v4.0 database. The results are presented through pseudobinary phase diagrams in Fig. 6. These diagrams offer insights into the behavior of Ag within the CrMnFeCoNi HEA system. Even at lower concentrations of Ag (5 at.%), the diagrams reveal that silver exhibits minimal solubility in the γ phase, with the mole fraction of Ag in the γ fcc phase nearly negligible. At lower temperatures, a pure fcc phase of Cantor prevails. However, as the concentration of Ag increases (10, 15, and 20 at.%), the diagrams point out a growing presence of the fcc Ag-phase, exceeding 25 at% Ag and approaching a similar order as the fcc Cantor one. Despite the increasing prevalence of the fcc Ag-phase, the compositional stability range of the fcc phase is observed to be limited, aligning with our experimental observations. Significantly, there is a discernible decrease in the fraction of the fcc phase, accompanied by an increase in the Ag fcc-phase, for all compositions containing silver. These modeling results find support in microstructural observations, where the alloy containing 10 at.% Ag exhibits both the fcc Cantor phase and the fcc Ag-phase. In summary, the thermodynamic modeling enhances our understanding of the phase behavior and compositional variations within the CrMnFeCoNiAg HEA system under investigation, providing valuable corroboration for our experimental outcomes.

We report on the impact of Ag addition on the phase composition and microstructural development of $CrMnFeCoNiAg_x$ HEA thin films deposited by magnetron co-sputtering, uncovering the intrinsic effect of Ag content and alloy behavior. We revealed that the introduction of Ag notably shifts the phase composition, promoting a distinctive bi-phased microstructure: This includes a well-crystallized Ag fcc phase alongside with a Cantor phase, emphasizing the significant role of Ag in altering the alloy's internal structure. Moreover, the occurrence of nanocrystalline morphologies and modulated structures through uniform and coherent silver nano-phase precipitation expresses to the profound impact of compositional tuning on the microstructural evolution of HEAs. Additionally, thermodynamic calculations confirmed the experimental observations, providing a predictive framework that captures the complex interplay between the configurational entropy and the mixing enthalpies, essential for phase stability and microstructural evolution in HEAs. Furthermore, the application of thermal treatment has elucidated the dynamic nature of these microstructures, revealing the conditions under which silver nanoprecipitates form and grow, offering insights into the thermal stability and phase transformation behaviors of these alloys.

CRediT authorship contribution statement

Salah-Eddine Benrazzouq: Writing – original draft, Methodology, Investigation, Data curation. **Abdelkrim Redjaimia:** Writing – review & editing, Investigation, Formal analysis. **Jaafar Ghanbaja:** Investigation. **Jean-Sébastien Lecomte:** Data curation. **Sylvie Migot:** Investigation. **Valentin A. Milichko:** Writing – review & editing, Supervision, Funding acquisition. **Jean-François Pierson:** Writing – review & editing, Supervision, Project administration, Conceptualization.

Declaration of competing interest

The authors declare that they have no known competing financial interests or personal relationships that could have appeared to influence the work reported in this paper.

Acknowledgments

This work was supported by the project CPJ: ANR-22-CPJ1–0010–01 of the French Agence Nationale de la Recherche. The Daυm competence center of IJL is deeply acknowledged for access to the UHV magnetron sputtering deposition facility and the Centre of Competences X-gamma for access to the X-ray diffraction system.

Supplementary materials

Supplementary material associated with this article can be found, in the online version, at doi:10.1016/j.scriptamat.2024.116521.

References

[1] W. Zhang, A. Chabok, B.J. Kooi, Y. Pei, Additive manufactured high entropy alloys: a review of the microstructure and properties, Mater. Des. 220 (2022) 110875, https://doi.org/10.1016/J.MATDES.2022.110875.

[2] J.W. Yeh, et al., Nanostructured high-entropy alloys with multiple principal elements: novel alloy design concepts and outcomes, Adv. Eng. Mater. 6 (5) (2004) 299–303, https://doi.org/10.1002/adem.200300567.

[3] Z. Wu, H. Bei, G.M. Pharr, E.P. George, Temperature dependence of the mechanical properties of equiatomic solid solution alloys with face-centered cubic crystal structures, Acta Mater 81 (2014) 428–441, https://doi.org/10.1016/J.ACTAMAT.2014.08.026.

[4] E.P. George, W.A. Curtin, C.C. Tasan, High entropy alloys: a focused review of mechanical properties and deformation mechanisms, Acta Mater 188 (2020) 435–474, https://doi.org/10.1016/J.ACTAMAT.2019.12.015.

[5] M.H. Chuang, M.H. Tsai, W.R. Wang, S.J. Lin, J.W. Yeh, Microstructure and wear behavior of AlxCo1.5CrFeNi1.5Tiy high-entropy alloys, Acta Mater 59 (16) (2011) 6308–6317, https://doi.org/10.1016/J.ACTAMAT.2011.06.041.

[6] S.K. Bachani, C.J. Wang, B.S. Lou, L.C. Chang, J.W. Lee, Fabrication of TiZrNbTaFeN high-entropy alloys coatings by HiPIMS: effect of nitrogen flow rate on the microstructural development, mechanical and tribological performance, electrical properties and corrosion characteristics, J. Alloys Compd. 873 (2021) 159605, https://doi.org/10.1016/J.JALLCOM.2021.159605.

[7] Z. Tang, T. Yuan, C.W. Tsai, J.W. Yeh, C.D. Lundin, P.K. Liaw, Fatigue behavior of a wrought Al0.5CoCrCuFeNi two-phase high-entropy alloy, Acta Mater 99 (2015) 247–258, https://doi.org/10.1016/J.ACTAMAT.2015.07.004.

[8] B. Gludovatz, A. Hohenwarter, D. Catoor, E.H. Chang, E.P. George, R.O. Ritchie, A fracture-resistant high-entropy alloy for cryogenic applications, Science (80-.) 345 (6201) (2014) 1153–1158, https://doi.org/10.1126/SCIENCE.1254581/SUPPL_FILE/GLUDOVATZ.SM.PDF.

[9] W.H. Kao, Y.L. Su, J.H. Horng, H.M. Wu, Effects of carbon doping on mechanical, tribological, structural, anti-corrosion and anti-glass-sticking properties of CrNbSiTaZr high entropy alloy coatings, Thin Solid Films 717 (2021) 138448, https://doi.org/10.1016/J.TSF.2020.138448.

[10] Y.F. Kao, S.K. Chen, T.J. Chen, P.C. Chu, J.W. Yeh, S.J. Lin, Electrical, magnetic, and Hall properties of AlxCoCrFeNi high-entropy alloys, J. Alloys Compd. 509 (5) (2011) 1607–1614, https://doi.org/10.1016/J.JALLCOM.2010.10.210.

[11] Y. Dong, et al., Transport properties of refractory high-entropy alloys with single-phase body-centered cubic structure, Scr. Mater. 231 (2023) 115464, https://doi.org/10.1016/J.SCRIPTAMAT.2023.115464.

[12] Y. Xin, et al., High-entropy alloys as a platform for catalysis: progress, challenges, and opportunities, ACS Catal 10 (19) (2020) 11280–11306, https://doi.org/10.1021/ACSCATAL.0C03617/ASSET/IMAGES/MEDIUM/CS0C03617_0016.GIF.

[13] Y. Sun, S. Dai, High-entropy materials for catalysis: a new frontier, Sci. Adv. 7 (20) (2021), https://doi.org/10.1126/SCIADV.ABG1600/ASSET/0B8BA449-7251-4A98-A8C7-157A2A1571C6/ASSETS/GRAPHIC/ABG1600-F6.JPEG.

[14] B. Ouyang, Y. Zeng, The rise of high-entropy battery materials, Nat. Commun. 15 (1) (2024) 1–5, https://doi.org/10.1038/s41467-024-45309-9. *2024 151*.

[15] A. Rashidy Ahmady, A. Ekhlasi, A. Nouri, M. Haghbin Nazarpak, P. Gong, A. Solouk, High entropy alloy coatings for biomedical applications: a review, Smart Mater. Manuf. 1 (2023) 100009, https://doi.org/10.1016/J.SMMF.2022.100009.

[16] J.W. Yeh, S.J. Lin, Breakthrough applications of high-entropy materials, J. Mater. Res. 33 (19) (2018) 3129–3137, https://doi.org/10.1557/JMR.2018.283.

[17] K.V.S. Thurston, B. Gludovatz, A. Hohenwarter, G. Laplanche, E.P. George, R. O. Ritchie, Effect of temperature on the fatigue-crack growth behavior of the high-entropy alloy CrMnFeCoNi, Intermetallics 88 (April) (2017) 65–72, https://doi.org/10.1016/j.intermet.2017.05.009.

[18] S.Y. Chen, et al., Phase transformations of HfNbTaTiZr high-entropy alloy at intermediate temperatures, Scr. Mater. 158 (2019) 50–56, https://doi.org/10.1016/j.scriptamat.2018.08.032.

[19] M. Feuerbacher, M. Heidelmann, C. Thomas, Hexagonal High-entropy Alloys, Mater. Res. Lett. 3 (1) (2014) 1–6, https://doi.org/10.1080/21663831.2014.951493.

[20] S. Sun, H. Liu, J. Hao, H. Yang, Microstructural evolution and corrosion behavior of CoCrFeNiAlxMn(1−x) dual-phase high-entropy alloy coatings prepared by laser cladding, J. Alloys Compd. 886 (2021) 161251, https://doi.org/10.1016/j.jallcom.2021.161251.

[21] Y. Zhang, et al., Concurrence of spinodal decomposition and nano-phase precipitation in a multi-component AlCoCrCuFeNi high-entropy alloy, J. Mater. Res. Technol. 8 (1) (2019) 726–736, https://doi.org/10.1016/J.JMRT.2018.04.020.

[22] J.L. Yuan, Z. Wang, X. Jin, P.D. Han, J.W. Qiao, Ultra-high strength assisted by nano-precipitates in a heterostructural high-entropy alloy, J. Alloys Compd. 921 (2022) 166106, https://doi.org/10.1016/J.JALLCOM.2022.166106.

[23] L. Liu, et al., Nanoprecipitate-strengthened high-entropy alloys, Adv. Sci. 8 (23) (2021), https://doi.org/10.1002/ADVS.202100870.

[24] Z. Fu, et al., A high-entropy alloy with hierarchical nanoprecipitates and ultrahigh strength, Sci. Adv. 4 (10) (2018) 8712–8724, https://doi.org/10.1126/SCIADV.AAT8712.

[25] B. Gwalani, et al., Cu assisted stabilization and nucleation of L12 precipitates in Al0.3CuFeCrNi2 fcc-based high entropy alloy, Acta Mater 129 (2017) 170–182, https://doi.org/10.1016/J.ACTAMAT.2017.02.053.

[26] Y.C. Hsu, C.L. Li, C.H. Hsueh, Modifications of microstructures and mechanical properties of CoCrFeMnNi high entropy alloy films by adding Ti element, Surf. Coatings Technol. 399 (June) (2020) 126149, https://doi.org/10.1016/j.surfcoat.2020.126149.

[27] S. Fang, et al., Microstructures and mechanical properties of CoCrFeMnNiVx high entropy alloy films, J. Alloys Compd. 820 (2020) 1–8, https://doi.org/10.1016/j.jallcom.2019.153388.

[28] Y.C. Hsu, C.L. Li, C.H. Hsueh, Effects of al addition on microstructures and mechanical properties of cocrfemnnialx high entropy alloy films, Entropy 22 (1) (2020) 2, https://doi.org/10.3390/e22010002.

[29] Y.H. Liang, C.L. Li, C.H. Hsueh, Effects of nb addition on microstructures and mechanical properties of Nbx-cocrfemnni high entropy alloy films, Coatings 11 (12) (2021), https://doi.org/10.3390/coatings11121539.

[30] T.H. Huang, C.H. Hsueh, Microstructures and mechanical properties of (CoCrFeMnNi)100-xMox high entropy alloy films, Intermetallics 135 (January) (2021) 107236, https://doi.org/10.1016/j.intermet.2021.107236.

[31] Y. Zhao, X. Zhang, H. Quan, Y. Chen, S. Wang, S. Zhang, Effect of Mo addition on structures and properties of FeCoNiCrMn high entropy alloy film by direct current magnetron sputtering, J. Alloys Compd. 895 (2022) 162709, https://doi.org/10.1016/j.jallcom.2021.162709.

[32] Y.F. Ye, Q. Wang, J. Lu, C.T. Liu, Y. Yang, High-entropy alloy: challenges and prospects, Mater. Today 19 (6) (2016) 349–362, https://doi.org/10.1016/j.mattod.2015.11.026.

[33] Y. Zhang, et al., Microstructures and properties of high-entropy alloys, Prog. Mater. Sci. 61 (November 2013) (2014) 1–93, https://doi.org/10.1016/j.pmatsci.2013.10.001.

[34] D. Raabe, The Materials Science behind Sustainable Metals and Alloys, Chem. Rev. 123 (5) (2023) 2436–2608, https://doi.org/10.1021/acs.chemrev.2c00799.

[35] B. Cantor, I.T.H. Chang, P. Knight, A.J.B. Vincent, Microstructural development in equiatomic multicomponent alloys, Mater. Sci. Eng. A 375–377 (1–2 SPEC. ISS) (2004) 213–218, https://doi.org/10.1016/j.msea.2003.10.257.

[36] L.L. Xiao, Z.Q. Zheng, S.W. Guo, P. Huang, F. Wang, Ultra-strong nanostructured CrMnFeCoNi high entropy alloys, Mater. Des. 194 (2020) 108895, https://doi.org/10.1016/J.MATDES.2020.108895.

[37] V. Maier-Kiener, B. Schuh, E.P. George, H. Clemens, A. Hohenwarter, Nanoindentation testing as a powerful screening tool for assessing phase stability of nanocrystalline high-entropy alloys, Mater. Des. 115 (2017) 479–485, https://doi.org/10.1016/J.MATDES.2016.11.055.

[38] A. Brognara, J.P. Best, P. Djemia, D. Faurie, G. Dehm, M. Ghidelli, Effect of composition and nanostructure on the mechanical properties and thermal stability of Zr100-xCux thin film metallic glasses, Mater. Des. 219 (2022) 110752, https://doi.org/10.1016/j.matdes.2022.110752.

[39] C.A. Schuh, T.C. Hufnagel, U. Ramamurty, Mechanical behavior of amorphous alloys, Acta Mater 55 (12) (2007) 4067–4109, https://doi.org/10.1016/j.actamat.2007.01.052.

[40] T.E. Whitfield, E.J. Pickering, L.R. Owen, C.N. Jones, H.J. Stone, N.G. Jones, The effect of Al on the formation and stability of a BCC-B2 microstructure in a refractory metal high entropy superalloy system, Materialia 13 (2020) 100858, https://doi.org/10.1016/j.mtla.2020.100858.

[41] D. Jin et al., "High-strength and energetic Al 2 Ti 6 Zr 2 Nb 3 Ta 3 high entropy alloy containing a cuboidal BCC/B2 coherent microstructure," 2022, doi: 10.1016/j.jallcom.2022.167546.

[42] V. Soni, et al., Phase inversion in a two-phase, BCC + B2, refractory high entropy alloy, Acta Mater 185 (2020) 89–97, https://doi.org/10.1016/j.actamat.2019.12.004.

[43] V. Soni, et al., Phase stability as a function of temperature in a refractory high-entropy alloy, J. Mater. Res. 33 (19) (2018) 3235–3246, https://doi.org/10.1557/jmr.2018.223.

[44] R. Wagner, R. Kampmann, and P.W. Voorhees, *Homogeneous Second-Phase Precipitation*. 2001. doi: 10.1002/352760264x.ch5.

[45] Q. Wang, et al., A cuboidal B2 nanoprecipitation-enhanced body-centered-cubic alloy Al0.7CoCrFe2Ni with prominent tensile properties, Scr. Mater. 120 (2016) 85–89, https://doi.org/10.1016/J.SCRIPTAMAT.2016.04.014.

[46] D. Isheim, O.C. Hellman, D.N. Seidman, F. Danoix, A. Bostel, D. Blavette, Atomic-scale study of a transition phase precipitate and its interfacial chemistry in an Fe−15 at.% Mo−5 at.% V Alloy, Microsc. Microanal. 7 (5) (2001) 424–434, https://doi.org/10.1007/s10005-001-0017-z.